Full-wavefield migration in the frequency-wavenumber domain

Shang Huang and Daniel O. Trad

ABSTRACT

Full wavefield migration (FWM) is an inversion-based migration method that can handle total wavefields, including primary reflections, surface-related multiples and internal multiples. Additional multiple energy can help with improving the subsurface imaging illumination. Previous work focuses on applying full wavefield forward modelling and imaging in the frequency-space domain. In this paper, full wavefield modelling and migration are performed in the frequency-wavenumber (FK) domain, since data in the FK domain is more straightforward to be extrapolated and processed. Phase shift plus interpolation is also combined in the forward modelling to simulate the complex wavefields generated from lateral velocity variations. A deconvolution imaging condition is considered in the imaging procedure to compute more accurate updated model perturbation. The result derived from using full wavefield migration in the frequency-wavenumber domain shows improved reflection response and amplitude spectrum compared with applying primary wavefield migration. This algorithm using multiple reflections provides higher frequency results and better lateral continuity.

INTRODUCTION

In the past, multiples are removed from the total wavefields using gridpoint responses before migration (Verschuur et al., 1992). However, migration of multiples, including surface-related multiples and internal multiples (Berkhout and Verschuur, 1994) can become a useful tool to add subsurface information. The least-squares inversion-based full-wavefield migration (FWM) in the frequency-space domain (Berkhout, 2014; Verschuur and Berkhout, 2015; Davydenko and Verschuur, 2016) starts to combine multiple energy iteratively to expand the imaging illumination and accuracy. This paper tries to apply the full-wavefield migration method in the frequency-wavenumber (FK) domain. One property for using the F-K domain is that it is straightforward to perform different orders of multiples. Moreover, computation in the FK domain can be a good start for the imaging angle-dependent reflectivity model. To handle lateral velocity variations in the model, phase shift plus interpolation (PSPI) is included for correct wavefield propagation. Furthermore, instead of using the cross-correlation imaging condition in the previous work, we use the deconvolution imaging condition to track a more accurate reflectivity model based on the predicted forward and backward wavefields.

THEORY

In this section, full wavefield migration in the frequency-wavenumber domain algorithm will be delineated in detail along with a basic framework shown in Figure 1.

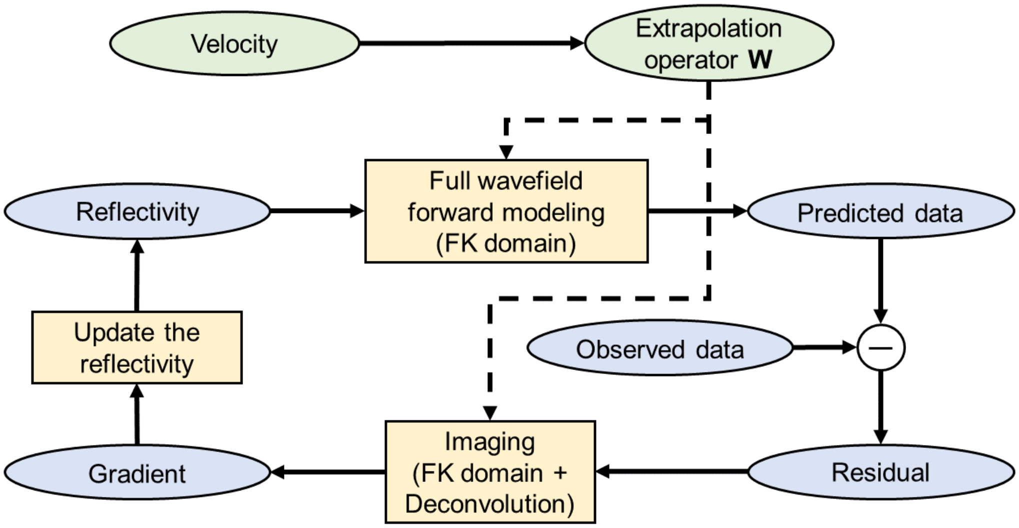

FIG. 1: Workflow for full wavefield migration (adapted from Davydenko and Verschuur (2016)) in the frequency-wavenumber domain

Forward modelling in FWM

Forward modelling in full wavefield migration (FWM) (Berkhout, 2014; Davydenko and Verschuur, 2016) delineates incoming and outgoing wavefields in terms of approaching a particular subsurface grid point or departing from it. By convention, a positive sign (+) represents the downward extrapolation, and a negative sign (-) means the upward propagation.

The downward extrapolated wavefield at depth z_m can be determined by the accumulation of primaries generated by a source on the surface $\vec{S}^+(z_0)$ and scattering wavefields obtained by secondary sources at the subsurface $\delta\vec{S}(z_n)$:

$$\vec{P}^+(z_m) = \sum_{n<m} \mathbf{W}(z_m, z_n)[\vec{S}^+(z_0) + \delta\vec{S}(z_n)] \tag{1}$$

where **W** represents extrapolation operators defined by phase shift extrapolation. The second sources or scattering wavefields $\delta\vec{S}(z_n)$ indicate the variation wavefields in both directions including transmission difference and reflections from opposite direction wavefields:

$$\delta\vec{S}(z_m) = \mathbf{R}^{\cup}(z_m)\vec{P}^+(z_m) + \mathbf{R}^{\cap}(z_m)\vec{P}^-(z_m) \tag{2}$$

For a media with small contrasts for shear-wave propagation velocity, reflectivities $\mathbf{R}^{\cup}$ and $\mathbf{R}^{\cap}$ can be assumed as transmission differences $\delta\mathbf{T}^+$ and $\delta\mathbf{T}^-$ respectively. Then, the upgoing wavefield at depth level z_m can also be determined by using the scattering term:

$$\vec{P}^-(z_m) = \sum_{n>m} \mathbf{W}(z_m, z_n)\delta\vec{S}(z_n) \tag{3}$$

When downward and upward extrapolations are obtained (Figure 2a and b), one can substitute equation 1 and equation 3 into equation 2 and update the scattering terms. Thus, for the next round-trip, the downgoing wavefields will include the source wavefield, and the reflections of previous upgoing wavefields at each depth layer (Figure 2c). Those reflections are also generating internal multiples between layers, which means that when the number of round-trips increases, a new order of surface multiples and internal multiples will be added to the propagation equations.

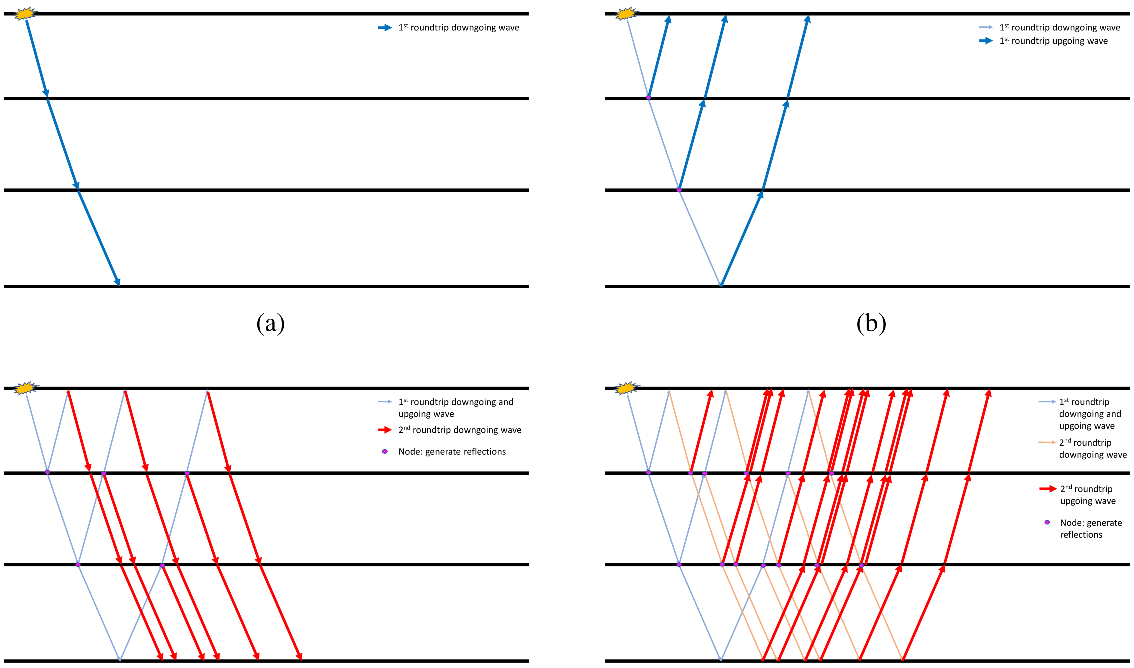

(a) (b)

(c) (d)

FIG. 2: (a) Downgoing wavefields at the first iteration. (b) Upward wavefields at the first iteration. (c) Downgoing wavefields at the second iteration. (d) Upward wavefields at the second iteration.

Forward modelling in FWM is reflectivity driven, while the background velocity only influences the propagation effect instead of the scattering effect. From the generated full wavefield, one can obtain the predicted data by choosing the upgoing wavefield on the surface, and then the residual between predicted data and observed data can be determined by subtraction. The residual wavefield then becomes the input for the imaging part in the algorithm.

Inversion-based imaging in FWM

As the workflow shown in Figure 1, during the iterative imaging process FWM uses the data residual to update the reflectivity coefficient for each layer. For this goal, similar to the objective function used in Davydenko and Verschuur (2016), but in this paper this function is applied in the frequency-wavenumber domain:

$$J = ||\Delta \mathbf{P}||_2^2 + f(\mathbf{R}) = ||\mathbf{P}_{obs} - \mathbf{P}_{mod}||_2^2 + f(\mathbf{R}), \tag{4}$$

where $\mathbf{P}_{obs}$ means the observed data on the surface, $\mathbf{P}_{mod}$ is predicted data and $\Delta\mathbf{P}$ is the difference between the observed and modeled data. $f(\mathbf{R})$ denotes the regularization term, for which the Cauchy function criterion (Amundsen, 1991) is used

$$f(\mathbf{R}(z_m)) = \frac{1}{2}\sum_{z_m} \ln(1 + \frac{\mathrm{diag}(\mathbf{R}(z_m))^H \mathrm{diag}(\mathbf{R}(z_m))}{\lambda^2}), \tag{5}$$

where $(*)^H$ means the complex conjugate, and the parameter λ corresponds to the scale parameter in the Cauchy distribution.

Instead of using the cross-correlation imaging condition mentioned in Davydenko and Verschuur (2016), we calculate the gradients of the objective function with respect to the above and below reflectivity coefficients by a deconvolution imaging condition (Valenciano and Biondi, 2003) form:

$$\mathbf{C}^{\cup}(z_m) = \frac{[\Delta\mathbf{P}^{-}(z_m)][\mathbf{P}^{+}(z_m)]^H}{[\mathbf{P}^{+}(z_m)][\mathbf{P}^{+}(z_m)]^H + \epsilon^2}, \tag{6}$$

$$\mathbf{C}^{\cap}(z_m) = \frac{[\Delta\mathbf{P}^{+}(z_m)][\mathbf{P}^{-}(z_m)]^H}{[\mathbf{P}^{-}(z_m)][\mathbf{P}^{-}(z_m)]^H + \epsilon^2} \tag{7}$$

where ϵ is a small value for stabilization. Based on Davydenko and Verschuur (2016) assumptions, $\Delta\mathbf{P}^{-}(z_m)$ and $\Delta\mathbf{P}^{+}(z_m)$ are computed by

$$\Delta\mathbf{P}^{-}(z_m) = [\mathbf{W}(z_0, z_m)]^H[\mathbf{P}_{obs}(z_0) - \mathbf{P}_{mod}(z_0)] \tag{8}$$

$$\Delta\mathbf{P}^{+}(z_m) = \sum_{n>m}[\mathbf{W}(z_n, z_m)]^H[\mathbf{R}^{\cup}(z_n)]\Delta\mathbf{P}^{-}(z_n) \tag{9}$$

$\Delta\mathbf{P}^{-}(z_m)$ (red solid line in Figure 3) represents the back-propagated upward residual, from data residual ($\Delta\mathbf{P}^{-}(z_0) = \mathbf{P}_{obs}(z_0)$-$\mathbf{P}_{mod}(z_0)$) on the surface. $\Delta\mathbf{P}^{+}(z_m)$ (blue solid line) denotes the back-propagated downward residual.

Equation 6 is the derivative with respect to upward reflectivity $\mathbf{R}^{\cup}(z_m)$. A corresponding sketch is shown in Figure 3, the numerator represents the cross-correlation of the upward receiver-side data residual $\Delta\mathbf{P}^{-}(z_m)$ (back-propagated to the depth level z_m by operator $\mathbf{W}(z_0, z_m)^H$, which is red dash line) with the forward modelled downgoing source-side wavefield $\mathbf{P}^{+}(z_m)$ (orange solid line).

Equation 7 illustrates the derivative with respect to the downward reflectivity $\mathbf{R}^{\cap}(z_m)$. For the numerator, the forward modelled upgoing source-side wavefield is cross-correlated with the data residual that was firstly back-propagated downwards at every depth-level located below the target depth level, multiplied by the reflectivity of these levels (below z_m) and finally back-propagated upwards to the target depth level z_m.

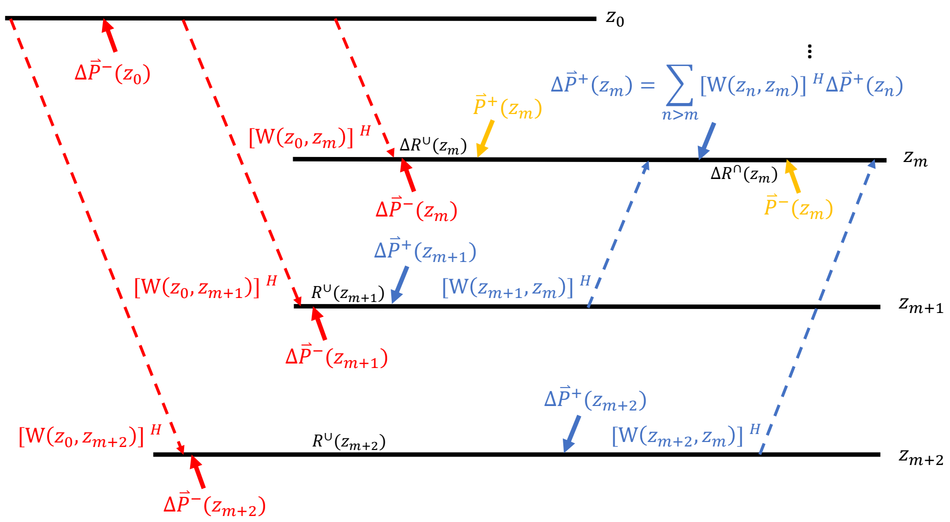

FIG. 3: Back-propagated upward residual (red solid lines) and downward residual (blue solid lines) are produced by operators (red and blue dash lines). Reflectivity updates of both sides can be projected by the product of forward-modelled wavefield (orange solid lines) and residuals.

To update reflectivity model, a model perturbation can be decided by summing over the frequency and wavenumber components of gradients which is corresponding to zero time deconvolution imaging condition:

$$\Delta\mathbf{R}(z_m) = \mathrm{diag}(\sum_k \sum_\omega \mathbf{C}(z_m)) + f'(\mathbf{R}(z_m)), \tag{10}$$

where the derivative of Cauchy criterion in terms of reflection coefficient should be

$$f'(\mathbf{R}(z_m)) = \frac{\mathrm{diag}(\mathbf{R}(z_m))}{1 + \lambda^{-2}\mathrm{diag}(\mathbf{R}(z_m))^H \mathrm{diag}(\mathbf{R}(z_m))} \tag{11}$$

Next, one can update the reflectivity matrix as follow:

$$\mathbf{R}_i^\cup(z_m) = \mathbf{R}_{i-1}^\cup(z_m) + \alpha\Delta\mathbf{R}_{i-1}^\cup(z_m), \tag{12}$$

where i denotes the current iteration number and α is determined by a line search method using the Wolfe condition. If there are small shear velocity variations in the media, one can use acoustic approximation that $\mathbf{R}^\cup = -\mathbf{R}^\cap$ to estimate the reflectivity coefficient of one-side only.

Note that downward reflectivity generates internal multiples as it translates the upgoing incoming wavefield downwards to the subsurface. By estimating the downward reflectivity, one can add internal multiple energy in imaging, whereas the upward reflectivity mainly provides primary information.

NUMERICAL EXAMPLES AND OBSERVATIONS

In this section, we ran two FWM tests (Table 1), one using the total data and another using only primaries. The first option uses surface multiples generated in the source side, and applies a scattering term to obtain internal multiples. The other mode considers only primary reflections.

Table 1: Two imaging modes in FWM method

Modes	Source side	Receiver side	ΔS
Full wavefield migration (total data) in the F-K domain	Source + Surface multiples	Total wavefields	Yes
Primary wavefield migration (primaries only) in the F-K domain	Source only	Primary wavefields	No

Horizontal-layered model

The test velocity and reflectivity models are shown in Figure 4, with a grid cell size of 5 meters in horizontal and vertical directions. A synthetic shot gather (Figure 7a) was modelled by the acoustic finite difference method (code adapted from Dr. Ali Fathalian) with the source located at the centre of the model on the surface. Prediction data was generated from full wavefield modelling whose frame is based on the phase shift method and one-way operators (code comes from Ferguson (2009)). A free surface boundary condition was applied in both the finite difference scheme and the full wavefield modelling. As shown in Figure 5a, a smooth velocity model was calculated by applying a Gaussian smoother to the original model. This smooth velocity was used for the calculation of the wavefield propagation operator. Thus, the initial low-resolution reflectivity (Figure 5b) obtained from this smoothed velocity will determine the initial scattering effects that will provide information to improve its resolution.

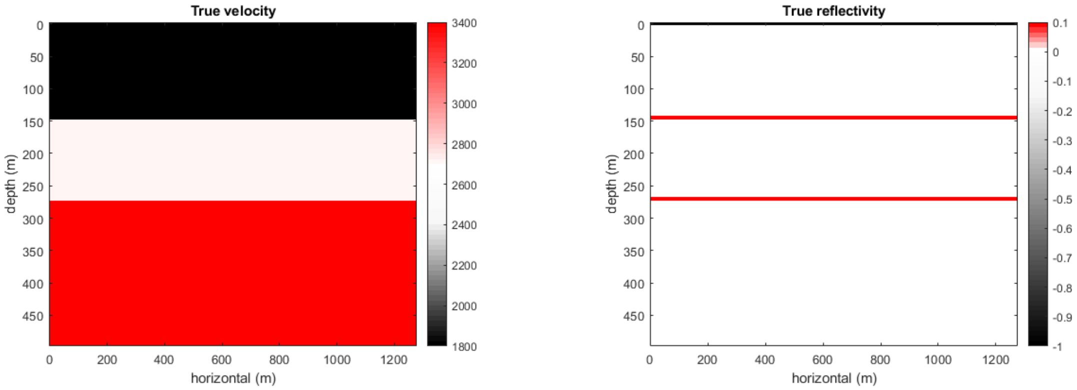

(a) (b)

FIG. 4: (a) True velocity. (b) True reflectivity.

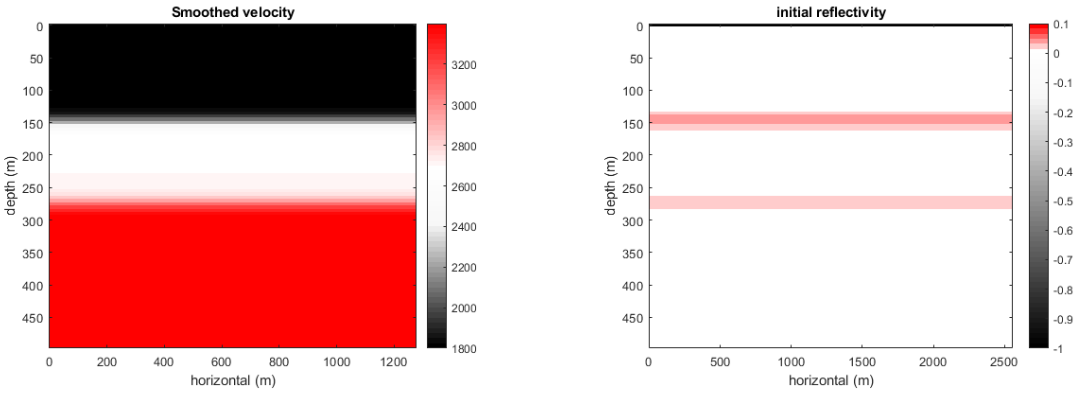

(a) (b)

FIG. 5: (a) Smoothed velocity. (b) Initial reflectivity.

For forward modelling in the first mode, Figure 6 illustrates both the space-time domain and frequency-wavenumber domain predicted data after the first and second iterations. F-K domain is more clear to see in which a new order of surface and internal multiples are added to data. Compared with the shot record (Figure 7a), the predicted data with total wavefields (Figure 7b) can predict most of the seismic events and add reflections from the subsurface and inter-bedding structure. The additional reflection information can help with recovering a better image for the second reflector. Predicted data in the second mode by PWM (Figure 7c) generated primary only, which corresponds to observed data, whereas there is no data amplitude after 0.45 seconds compared with full-wavefield data where the surface and internal multiples should exist.

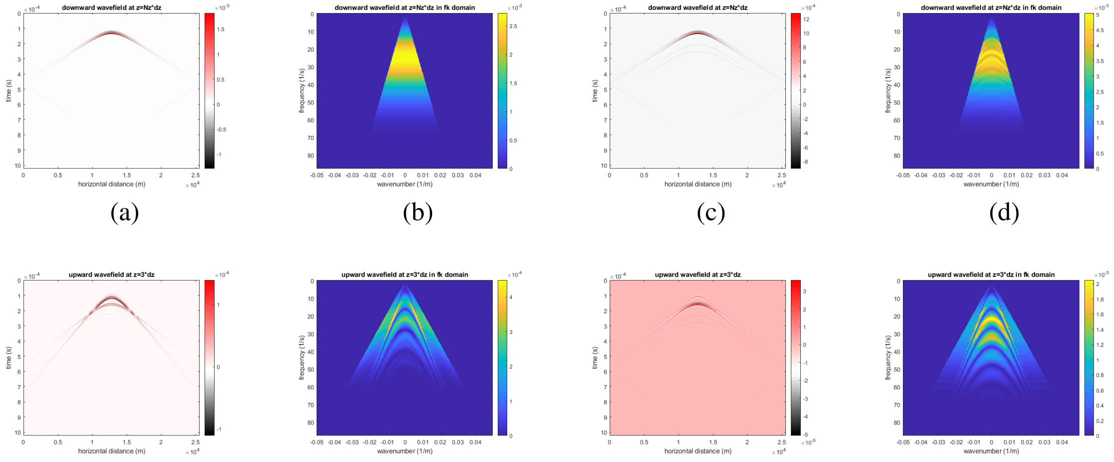

(a) (b) (c) (d)

(e) (f) (g) (h)

FIG. 6: (a) Downgoing wavefield recorded at the model bottom after the first iteration. (b) FK domain downgoing wavefield at the model bottom after the first iteration. (c) Downgoing wavefield recorded at the model bottom after two iterations. (d) FK domain downgoing wavefield at the model bottom after two iterations. (e) Upgoing wavefield recorded at the source location after the first iteration. (f) FK domain upgoing wavefield at the source location after the first iteration. (g) Upgoing wavefield recorded at the source location after two iterations. (h) FK domain upgoing wavefield at the source location after two iterations.

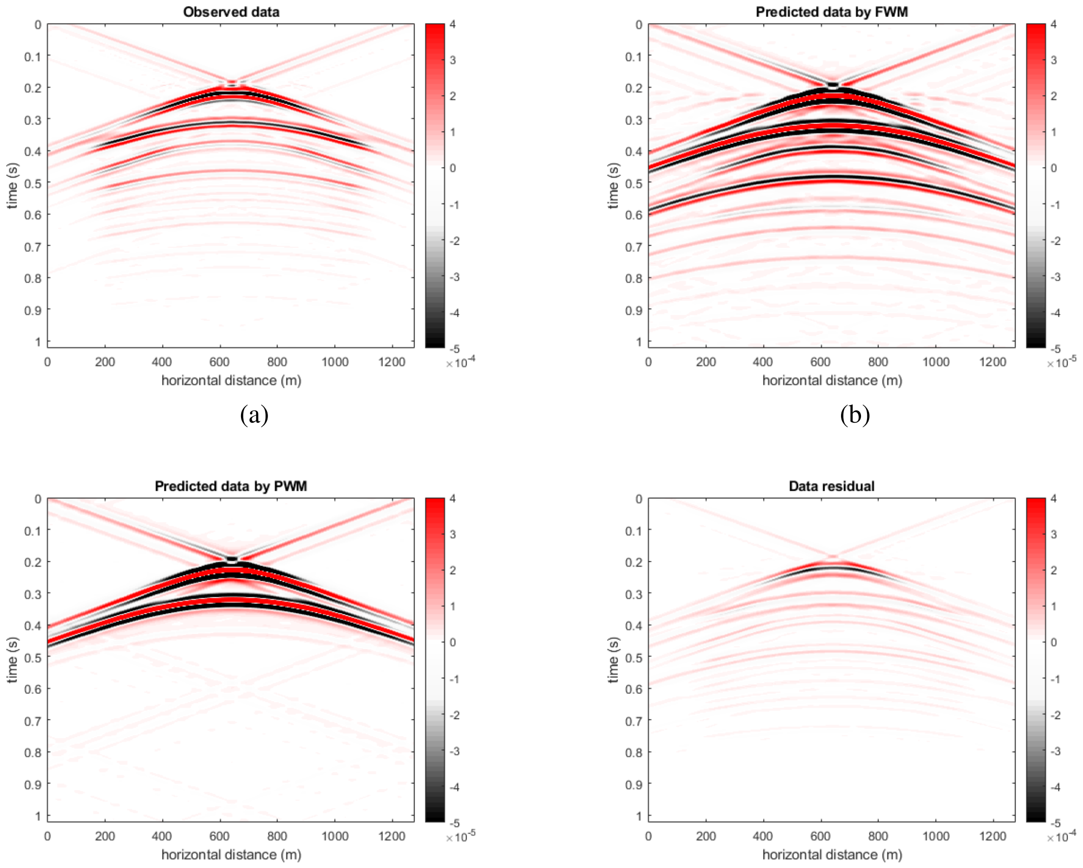

(a) (b)

(c) (d)

FIG. 7: (a) Observation data. (b) Predicted data by FWM after 5 iterations. (c) Predicted data by PWM. (d) Data residual between (a) and (b).

The updated reflection coefficient after using full-wavefield migration (red line in Figure 8) was more accurate and close to the true reflection coefficient values than applying primary only (blue line in Figure 8). Precisely, at depth 270 meters, FWM improved reflectivity coefficient amplitude and was 12.2% larger than PWM and 450.0% larger than the initial model, which means FWM can provide more information from the surface and internal multiples for migration.

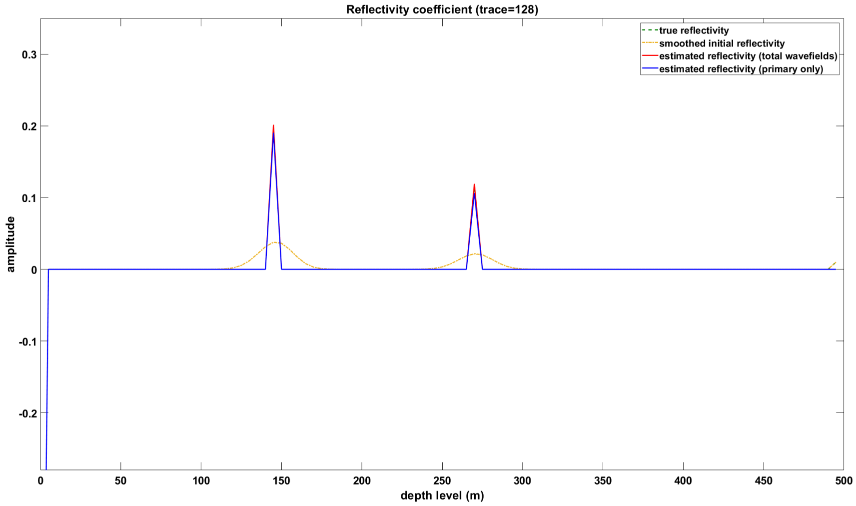

FIG. 8: One trace reflectivity comparison between FWM and PWM methods.

A normalized error plot in Figure 9 shows that after five iterations in the FWM approach, the error between observed data and predicted data decreases to 0.55 compared with a high convergence rate at the first three iterations.

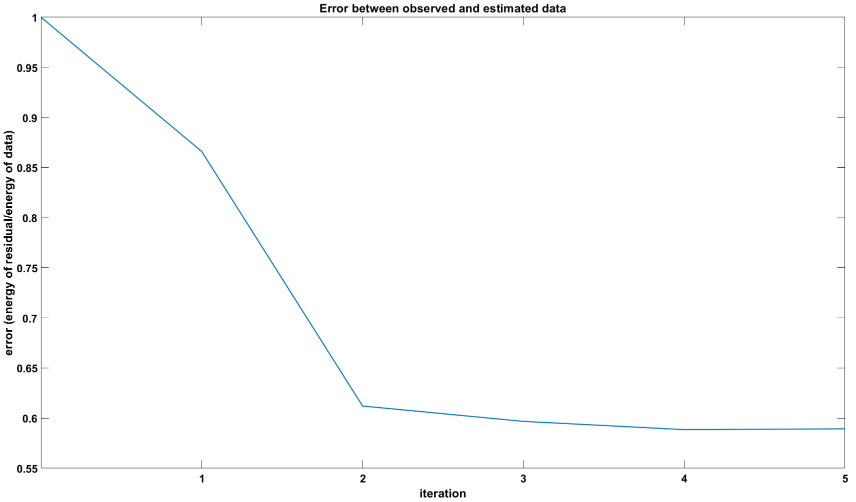

FIG. 9: Normalized misfit between observed and predicted data after 5 iterations.

Left part of the Marmousi model

For this example, we extracted the left part of the Marmousi model because the velocity model has a smooth lateral variation. One source was located at the centre of the model on the surface. Our code, for now, can handle with smooth lateral velocity change in the acoustic media. In the future, we will consider the angle-dependent reflectivity case, which can be performed on the steeper subsurface layers.

The new model (Figure 10) had 128x150 grid points with a 5 meters interval in both horizontal and vertical directions. A smoothed velocity model (Figure 11) was computed using a Gaussian smoother with a half-width equal to 10 gridpoints.

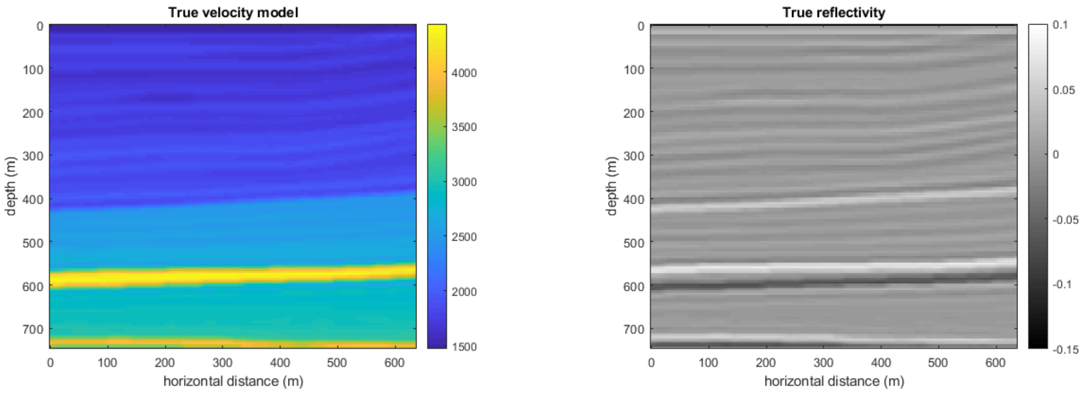

(a) (b)

FIG. 10: (a) True velocity. (b) True reflectivity.

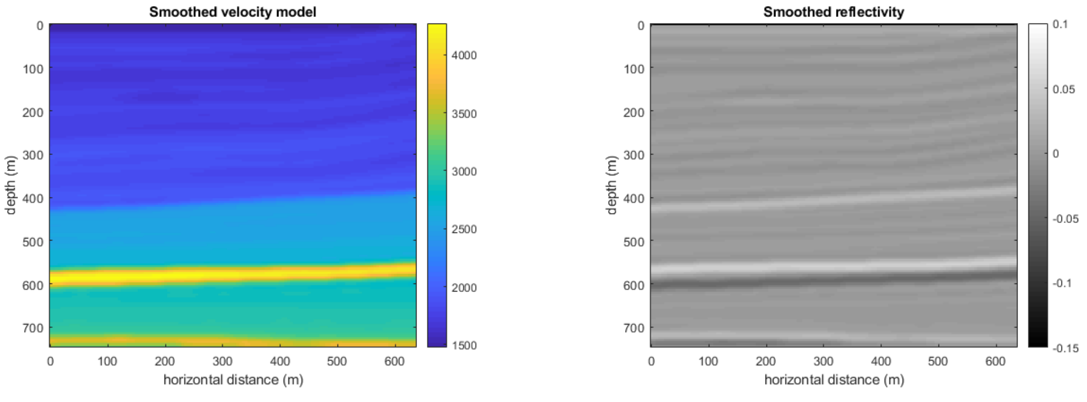

(a) (b)

FIG. 11: (a) Smoothed velocity. (b) Smoothed reflectivity.

The deconvolution imaging condition is used in this project because it can helps with predicting correct subsurface image compared with using cross-correlation. For example, above reflectivity update **dRa** and below reflectivity update **dRb** calculated by deconvolution imaging condition contains thin layers prediction in Figure 12a and b whereas cross-correlation lacks the shallow structure information and has low resolution in Figure 13a and b. After combining both above and below reflectivity update matrix, the result in Figure 12c is showing clear thin layer boundaries and the trend of subsurface structures. Cross-correlation imaging condition result (Figure 13c) will be misleading the prediction image because the update matrix has negative value for almost all the layer reflection coefficient and shows horizontal-layered structure which is incorrect compared with true reflectivity model.

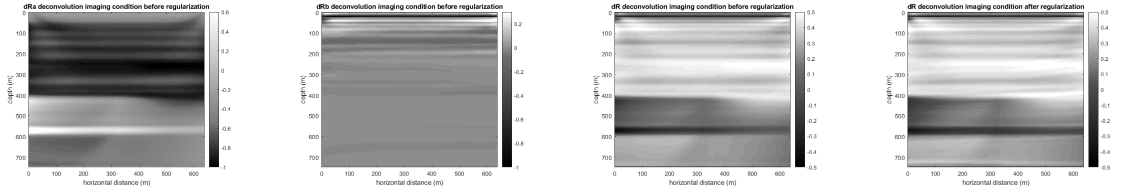

(a) (b) (c) (d)

FIG. 12: Deconvolution imaging condition for estimating (a) above reflectivity update and (b) below reflectivity update. Total reflectivity update (c) before and (d) after regularization.

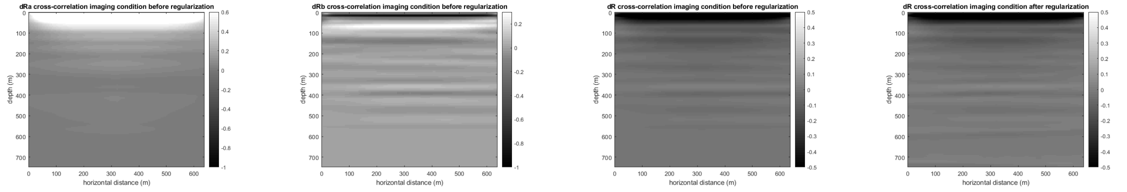

(a) (b) (c) (d)

FIG. 13: Cross-correlation imaging condition for estimating (a) above reflectivity update and (b) below reflectivity update. Total reflectivity update (c) before and (d) after regularization.

After using full wavefield migration, the estimation result had higher reflectivity amplitude (Figure 14b red line in Figure 15) compared with using primary wavefield migration (Figure 14a and blue line in Figure 15). Some details in the structure can also be recovered. For example, at a depth between 100 to 300 meters and 400 to 550 meters, thin layers' boundaries were clearly estimated.

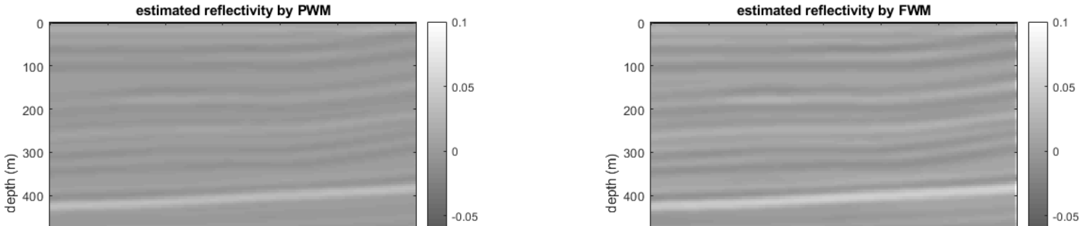

(a) (b)

FIG. 14: (a) Estimated reflectivity calculated by PWM. (b) Estimated reflectivity calculated by FWM.

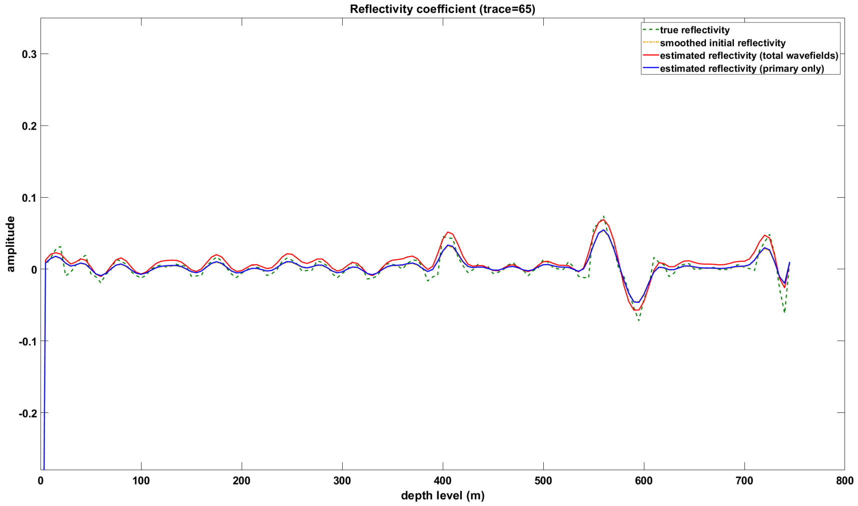

FIG. 15: One trace reflectivity comparison between PWM and FWM.

A normalized amplitude spectrum comparison between true shot record, PWM result and FWM result is shown in Figure 16. The amplitude spectrum plots calculated by three methods lacked 0 to 4 Hz low-frequency information. The high-frequency limitation was around 125 Hz. FWM result (red line in Figure 16) had better performance within the bandwidth compared with PWM result (blue line in Figure 16). After five iterations of FWM result, the signal-to-noise ratio was 88.76 %, and that of PWM result was 73.84 %.

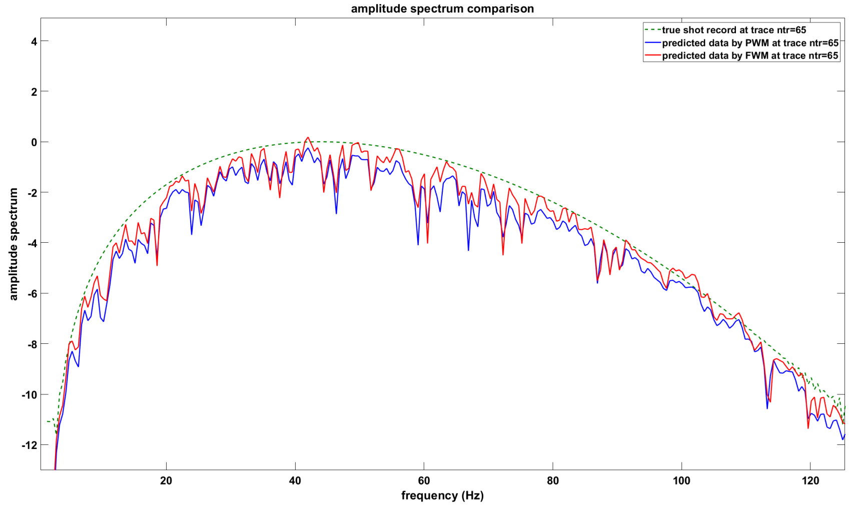

FIG. 16: Amplitude spectrum comparison.

When we compare the prediction data by two methods in the frequency-wavenumber domain, full wavefield modelling (Figure 17c) can predict more events generated from the subsurface layers with higher resolution compared with primary wavefield modelling (Figure 17b). Additionally, Figure 17c has a wider frequency band after 60 Hz and higher amplitude spectrum which is corresponding the result in Figure 16. However, when we compare Figure 17b and c with finite-difference generated observation data (Figure 17a), even though after 5 iterations, full wavefield modelling needs more iterations to improve the events prediction and correct the amplitude as well as the phase information, which might be solved by optimizing the phase shift plus interpolation during the forward modelling.

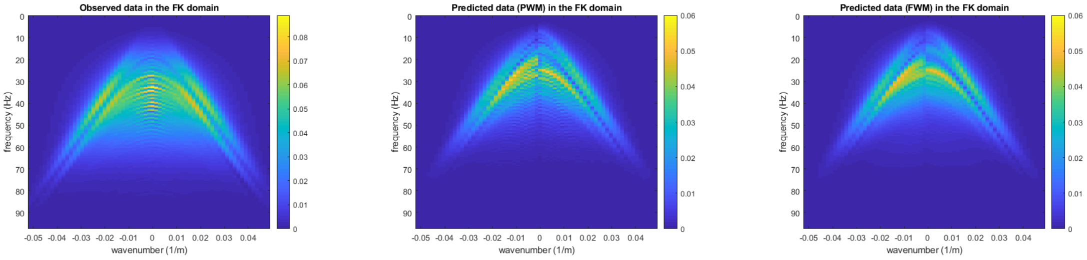

(a) (b) (c)

FIG. 17: (a) Observed data in the F-K domain. (b) Primary wavefield modelling in the F-K domain. (c) Full wavefields modelling in the F-K domain.

The normalized misfit (Figure 18) between observed and predicted data has a similar feature as mentioned in the previous example that the residual decreases to less than 0.7 after 5 iterations with a high convergence rate at the first two iterations.

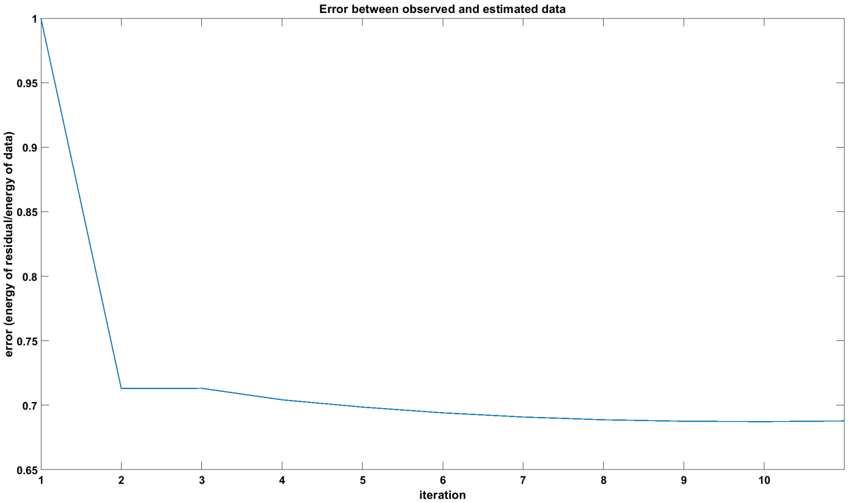

FIG. 18: Normalized error analysis of full wavefield migration after 5 iterations.

CONCLUSIONS

This paper has examined the uses of surface and internal multiples for full wavefield migration in the frequency-wavenumber domain compared with using primary wavefield migration. Full wavefield migration can reconstruct the reflectivity model's amplitudes in the horizontal-layered model and slight lateral velocity variations. The result is more accurate than applying primary wavefield migration. Migration in the frequency-wavenumber domain shows the improvement of a new order of multiples after each iteration, which is straightforward and can avoid artifacts generated from model boundaries compared with calculating in the space-time domain. Given wide offsets and a good initial background model, the deconvolution imaging condition can improve to predict subsurface layer locations with fewer artifacts.

FUTURE WORK

In future work, we should correct the amplitude and phase information showing in the F-K domain by using a wrap-around attenuation operator or optimizing the phase shift plus interpolation during the forward modelling. The next step is trying to reduce the computational cost due to the three-dimensional data structure. Furthermore, we need to consider angle-dependent reflectivity or angle gathers into the migration process for better imaging results.

ACKNOWLEDGEMENTS

The authors would like to thank the sponsors of CREWES for continued support. This work was funded by CREWES industrial sponsors, China Scholarship Council (CSC), NSERC (Natural Science and Engineering Research Council of Canada) through the grants CRDPJ 461179-13 and CRDPJ 543578-19. We also thank Dr. Samuel Gray, Kristof De Meersman, Xin Fu, Qi Hu and Ziguang Su for valuable discussions, and Dr. Ali Fathalian for his finite-difference modelling code on the Matlab.

REFERENCES

Amundsen, L., 1991, Comparison of the least-squares criterion and the cauchy criterion in frequency-wavenumber inversion: Geophysics, **56**, No. 12, 2027–2035.

Berkhout, A., 2014, An outlook on the future of seismic imaging, part ii: Full-wavefield migration: Geophysical Prospecting, **62**, No. 5, 931–949.

Berkhout, A., and Verschuur, D. J., 1994, Multiple technology: Part 2, migration of multiple reflections, *in* SEG Technical Program Expanded Abstracts 1994, Society of Exploration Geophysicists, 1497–1500.

Davydenko, M., and Verschuur, D., 2016, Full-wavefield migration: using surface and internal multiples in imaging: Geophysical Prospecting, **65**, No. 1, 7–21.

Ferguson, R., 2009, Isotropic phase shift extrapolation (stationary) source code: CREWES Matlab Toolbox.

Valenciano, A. A., and Biondi, B., 2003, 2-d deconvolution imaging condition for shot-profile migration, *in* SEG Technical Program Expanded Abstracts 2003, Society of Exploration Geophysicists, 1059–1062.

Verschuur, D., and Berkhout, A., 2015, From removing to using multiples in closed-loop imaging: The Leading Edge, **34**, No. 7, 744–759.

Verschuur, D. J., Berkhout, A., and Wapenaar, C., 1992, Adaptive surface-related multiple elimination: Geophysics, **57**, No. 9, 1166–1177.